Sunkyu Yu, Xianji Piao and Namkyoo Park

Supplementary Information for "Topologically protected optical signal processing using parity-time-symmetric oscillation quenching"

NOTE A. TYPES OF INTENSITY-DEPENDENT NONLINEARITY FUNCTIONS

Intensity-dependent nonlinearities can be classified into saturable responses [1, 2] and multiphoton processes [3, 4] such as two- or three-photon absorption (TPA [5] or 3PA [6]) and emission (TPE [7] or 3PE [8]). Saturable responses indicate a decrease in a gain or loss coefficient as the light intensity increases, which is observed in the gain saturation of lasers and amplifiers [1, 9] and saturable absorption [2, 10, 11]. These responses are described by the nonlinearity function $N(I) = \eta / [1 + (I/I_s)]$, where $\eta > 0$ for saturable gain, $\eta < 0$ for saturable loss, and I_s denotes the saturation intensity. On the other hand, multiphoton absorption and emission processes exhibit nonlinearity functions with polynomial expressions, as shown in the TPA and TPE with $N(I) = \eta I$ [5, 7] and the 3PA and 3PE with $N(I) = \eta I^2$ [6, 8], where $\eta > 0$ for emission and $\eta < 0$ for absorption. Figure S1 shows the $N(I)$ functions for different types of intensity-dependent optical nonlinearities.

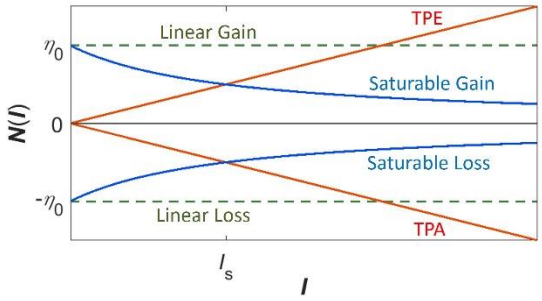

Fig. S1. Nonlinearity functions $N(I)$ of intensity-dependent optical nonlinearities: red lines for TPA and TPE with $N(I) = \pm\eta_0 I$ and blue lines for saturable gain and loss with $N(I) = \pm\eta_0 / [1 + (I/I_s)]$. The green dashed lines represent linear gain and loss with $N(I) = \pm\eta_0$. We set $\eta_0 > 0$ for all cases.

NOTE B. PHASE EQUATIONS

By replacing a_m with $I_m^{1/2}\exp(i\varphi_m)$ in Eq. (1) and employing Eq. (2) in the main text, we achieve

$$\sqrt{I_1}\frac{d\varphi_1}{dt} = \omega_0\sqrt{I_1} - iN_1\sqrt{I_1} + \kappa\sqrt{I_2}e^{-i\theta} + i\frac{N_1 I_1 + \kappa\sqrt{I_1 I_2}\sin\theta}{\sqrt{I_1}},$$
$$\sqrt{I_2}\frac{d\varphi_2}{dt} = \omega_0\sqrt{I_2} - iN_2\sqrt{I_2} + \kappa\sqrt{I_1}e^{+i\theta} + i\frac{N_2 I_2 - \kappa\sqrt{I_1 I_2}\sin\theta}{\sqrt{I_2}}. \quad \text{(S1)}$$

Because the imaginary parts of Eq. (S1) are zero, an equation for the field phase φ_m inside each resonator is derived, as

$$\sqrt{I_1}\frac{d\varphi_1}{dt} = \omega_0\sqrt{I_1} + \kappa\sqrt{I_2}\cos\theta,$$
$$\sqrt{I_2}\frac{d\varphi_2}{dt} = \omega_0\sqrt{I_2} + \kappa\sqrt{I_1}\cos\theta. \quad \text{(S2)}$$

The time derivatives of the phase functions $d\varphi_{1,2}(t)/dt$ represent the instantaneous frequencies of the fields in resonators 1 and 2, correspondingly. The static condition of the phase difference $\theta(t) = \varphi_1(t) - \varphi_2(t) = \theta_s$ is found in Eq. (S2), which will be discussed later in Note G.

NOTE C. PHASE DIFFERENCE FUNCTION

With the resonator synchronization that achieves $da_m/dt = i\omega a_m$ and static $N_m(I_m)$, Eq. (1) in the main text becomes an eigenvalue equation of general PT-symmetric two-level systems [12, 13]

$$\begin{bmatrix} \omega_0 - iN_1(I_1) & \kappa \\ \kappa & \omega_0 - iN_2(I_2) \end{bmatrix} \begin{bmatrix} a_1 \\ a_2 \end{bmatrix} = \omega \begin{bmatrix} a_1 \\ a_2 \end{bmatrix}. \tag{S3}$$

From Eq. (S3), a_1/a_2 of each eigenmode is obtained as

$$\frac{a_1}{a_2} = i\frac{(N_2 - N_1)}{2\kappa} \pm \sqrt{1 - \left[\frac{(N_2 - N_1)}{2\kappa}\right]^2}, \tag{S4}$$

which is plotted in Fig. S2 with various values of parameter $\gamma = [N_2(I_2) - N_1(I_1)]/(2\kappa)$.

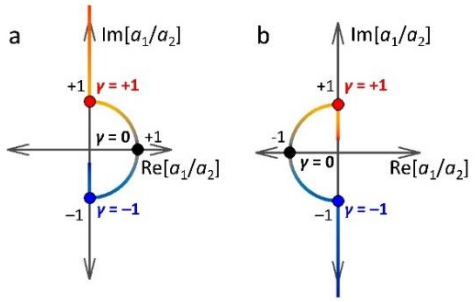

Fig. S2. The ratio between each resonator field near equilibria. (a,b) The ratio a_1/a_2 of two steady-state eigenmodes with various values of γ. The blue curve is for $\gamma < 0$, and the red curve is for $\gamma \geq 0$.

Depending on the magnitude of γ, Eq. (S4) is divided into

$$\frac{a_1}{a_2} = \begin{cases} i\gamma \pm \sqrt{1-\gamma^2} & \text{if} \quad |\gamma| \leq 1, \\ i\left(\gamma \pm \sqrt{\gamma^2 - 1}\right) & \text{if} \quad |\gamma| > 1, \end{cases} \tag{S5}$$

with $|a_1/a_2| = 1$ for $|\gamma| \leq 1$ (unbroken PT symmetry) and $|a_1/a_2| = |\gamma \pm (\gamma^2 - 1)^{1/2}|$ for $|\gamma| > 1$ (broken PT symmetry). From $a_1/a_2 = |a_1/a_2|\exp(i\theta_s)$, we obtain $\sin\theta_s = |a_2/a_1|\mathrm{Im}(a_1/a_2)$, which leads to Eq. (3) in the main text. Although θ_s, the angle in the complex plane in Fig. S2, depends on $N_{1,2}(I_{1,2})$, the values of $\sin\theta_s = \sin(\pi - \theta_s)$ in both eigenmodes are always the same.

NOTE D. JACOBIAN MATRIX AT EQUILIBRIUM

From Eq. (2) of the form $dI_1/dt = F_1(I_1, I_2)$ and $dI_2/dt = F_2(I_1, I_2)$ in the main text, each component of the 2×2 Jacobian matrix A is $A_{i,j} = \partial F_i/\partial I_j$, leading to

$$A = \begin{bmatrix} 2N_1 + 2N_1'I_1 + \kappa\sqrt{\frac{I_2}{I_1}}\sin\theta + 2\kappa\sqrt{I_1I_2}\frac{\partial\sin\theta}{\partial I_1} & \kappa\sqrt{\frac{I_1}{I_2}}\sin\theta + 2\kappa\sqrt{I_1I_2}\frac{\partial\sin\theta}{\partial I_2} \\ -\kappa\sqrt{\frac{I_2}{I_1}}\sin\theta - 2\kappa\sqrt{I_1I_2}\frac{\partial\sin\theta}{\partial I_1} & 2N_2 + 2N_2'I_2 - \kappa\sqrt{\frac{I_1}{I_2}}\sin\theta - 2\kappa\sqrt{I_1I_2}\frac{\partial\sin\theta}{\partial I_2} \end{bmatrix}. \tag{S6}$$

When the state of the system approaches equilibrium, the time-varying phase difference $\theta(t)$ and the related derivative $\partial\sin\theta(t,I_1,I_2)/\partial I_m$ converge to the static function $\theta_s(I_1,I_2)$ and the derivative $\partial\sin\theta_s(I_1,I_2)/\partial I_m$, respectively. At equilibrium ($I_1 = I_{1E}$ and $I_2 = I_{2E}$), Eq. (4) in the main text derives

$$\kappa\sqrt{\frac{I_{2E}}{I_{1E}}}\sin\theta_s(I_{1E},I_{2E}) = -N_1(I_{1E}),$$
$$\kappa\sqrt{\frac{I_{1E}}{I_{2E}}}\sin\theta_s(I_{1E},I_{2E}) = N_2(I_{2E}). \tag{S7}$$

By substituting Eq. (S7) into Eq. (S6) and using the θ_s function from the equilibrium condition, the Jacobian matrix A at equilibrium (I_{1E}, I_{2E}) is obtained, as

$$A = \begin{bmatrix} N_1(I_{1E}) + 2N_1'(I_{1E})I_{1E} + 2\kappa\sqrt{I_{1E}I_{2E}}\left.\frac{\partial\sin\theta_s}{\partial I_1}\right|_{I_{1E,2E}} & N_2(I_{2E}) + 2\kappa\sqrt{I_{1E}I_{2E}}\left.\frac{\partial\sin\theta_s}{\partial I_2}\right|_{I_{1E,2E}} \\ N_1(I_{1E}) - 2\kappa\sqrt{I_{1E}I_{2E}}\left.\frac{\partial\sin\theta_s}{\partial I_1}\right|_{I_{1E,2E}} & N_2(I_{2E}) + 2N_2'(I_{2E})I_{2E} - 2\kappa\sqrt{I_{1E}I_{2E}}\left.\frac{\partial\sin\theta_s}{\partial I_2}\right|_{I_{1E,2E}} \end{bmatrix}. \tag{S8}$$

NOTE E. EQUILIBRIUM AND JACOBIAN MATRIX OF UNBROKEN PT

For unbroken PT symmetry that satisfies $\sin\theta_E(I_{1E}, I_{2E}) = [N_2(I_{2E}) - N_1(I_{1E})]/(2\kappa)$, Eq. (4) in the main text becomes

$$N_1(I_{1E})I_{1E} = -N_2(I_{2E})I_{2E} = -\frac{\sqrt{I_{1E}I_{2E}}}{2}\left[N_2(I_{2E}) - N_1(I_{1E})\right]. \tag{S9}$$

The emergence of a nontrivial equilibrium with $I_{1E,2E} \neq 0$ and $N_{1,2} \neq 0$ requires $I_{1E} = I_{2E} = I_{HE}$, which represents the homogeneous steady state (HSS) [14]. The obtained HSS condition simplifies Eq. (S9) to $N_1(I_{HE}) = -N_2(I_{HE})$, which corresponds to balanced nonlinear gain and loss. The intensity value I_{HE} of the equilibrium is then obtained from the specific mathematical forms of N_1 and N_2, which are determined by the type of optical nonlinearity. The condition of unbroken PT symmetry is also simplified as $|\kappa| \geq |N_1(I_{HE})| = |N_2(I_{HE})|$.

Using the conditions of $I_{1E} = I_{2E} = I_{HE}$, $\partial\sin\theta_E/\partial I_1 = -N_1'/(2\kappa)$, and $\partial\sin\theta_E/\partial I_2 = N_2'/(2\kappa)$, the Jacobian matrix A for unbroken PT symmetry is derived from Eq. (S8) as

$$A = \begin{bmatrix} N_1(I_{HE}) + N_1'(I_{HE})I_{HE} & N_2(I_{HE}) + N_2'(I_{HE})I_{HE} \\ N_1(I_{HE}) + N_1'(I_{HE})I_{HE} & N_2(I_{HE}) + N_2'(I_{HE})I_{HE} \end{bmatrix}. \tag{S10}$$

For nontrivial equilibria ($I_{HE} \neq 0$), Eq. (S10) results in a single eigenvalue $\lambda_{HE} = [N_1'(I_{HE}) + N_2'(I_{HE})]I_{HE}$ due to the degeneracy of the matrix A with the HSS condition $N_1(I_{HE}) = -N_2(I_{HE})$.

NOTE F. EQUILIBRIUM AND JACOBIAN MATRIX OF BROKEN PT

For broken PT symmetry that satisfies $\sin\theta_E(I_{1E}, I_{2E}) = \mathrm{sgn}([N_2(I_{2E}) - N_1(I_{1E})]/(2\kappa))$, Eq. (4) in the main text becomes

$$N_1(I_{1E})I_{1E} = -N_2(I_{2E})I_{2E} = \begin{cases} +\kappa\sqrt{I_{1E}I_{2E}} & \text{if } \dfrac{N_2(I_{2E}) - N_1(I_{1E})}{2\kappa} < 0 \\ -\kappa\sqrt{I_{1E}I_{2E}} & \text{if } \dfrac{N_2(I_{2E}) - N_1(I_{1E})}{2\kappa} \geq 0 \end{cases}, \tag{S11}$$

It is noted that Eq. (S11) leads to the condition of $N_1(I_{1E})N_2(I_{2E}) = -\kappa^2$. The intensity ratio at the equilibrium $I_{2E}/I_{1E} = -N_1(I_{1E})/N_2(I_{2E})$ does not need to be unity, generally resulting in the

inhomogeneous steady state (IHSS) [15]. Notably, the condition of broken PT symmetry is automatically satisfied with $N_1(I_{1E})N_2(I_{2E}) = -\kappa^2$, regardless of the value of κ.
For broken PT symmetry, $\sin\theta_E$ is constant (Eq. (3) in the main text); thus, $\partial\sin\theta_E/\partial I_1 = \partial\sin\theta_E/\partial I_2 = 0$. The Jacobian matrix A for broken PT symmetry is derived from Eq. (S8) as

$$A = \begin{bmatrix} N_1(I_{1E}) + 2N_1'(I_{1E})I_{1E} & N_2(I_{2E}) \\ N_1(I_{1E}) & N_2(I_{2E}) + 2N_2'(I_{2E})I_{2E} \end{bmatrix}, \tag{S12}$$

which has two eigenvalues $\lambda_{\pm E} = [N_1(I_{1E}) + N_2(I_{2E})]/2 + N_1'(I_{1E})I_{1E} + N_2'(I_{2E})I_{2E} \pm \rho^{1/2}/2$, and ρ is defined as

$$\rho = \left[N_1(I_{1E}) - N_2(I_{2E}) + 2\left(N_1'(I_{1E})I_{1E} - N_2'(I_{2E})I_{2E} \right) \right]^2 + 4N_1(I_{1E})N_2(I_{2E}). \tag{S13}$$

NOTE G. PROOF OF STATIC PHASE DIFFERENCE

In the analysis of the equilibrium and its stability, we employed the static phase difference condition $\theta(t,I_1,I_2) = \theta_s(I_1,I_2)$ for separate analysis of the phases of PT symmetry. This condition requires $d\theta/dt = d(\varphi_1 - \varphi_2)/dt = 0$. From Eq. (S2), we achieve

$$\frac{d(\varphi_1 - \varphi_2)}{dt} = \kappa\left(\sqrt{\frac{I_2}{I_1}} - \sqrt{\frac{I_1}{I_2}} \right)\cos\theta. \tag{S14}$$

Therefore, $d\theta/dt = 0$ for the equilibria in all phases of PT symmetry, due to the conditions of (i) $I_{1E} = I_{2E} = I_{HE}$ for unbroken PT symmetry and (ii) $\cos\theta_E(I_{1E}, I_{2E}) = 0$ from $\sin\theta_E(I_{1E}, I_{2E}) = \pm 1$ for broken PT symmetry.

NOTE H. ANALYTICAL SOLUTIONS OF THE EXAMPLE SYSTEM

For the set of the nonlinearity functions $N_1(I_1) = \eta_{11}I_1 + \eta_{10}$ and $N_2(I_2) = \eta_{20}$, the relation $N_1(I_{HE}) = -N_2(I_{HE})$ for unbroken PT symmetry derives the HSS equilibrium, as $I_{HE} = -(\eta_{10} + \eta_{20})/\eta_{11}$. Due to $N_1'(I_{HE}) = \eta_{11}$ and $N_2'(I_{HE}) = 0$, the Jacobian eigenvalue becomes $\lambda_{HE} = -(\eta_{10} + \eta_{20})$. The necessary condition of unbroken PT symmetry $|\kappa| \geq |N_1(I_{HE})| = |N_2(I_{HE})|$ also becomes $\kappa \geq |\eta_{20}|$ with $\kappa \geq 0$.
The relations of $N_1(I_{1E})N_2(I_{2E}) = -\kappa^2$ and $I_{2E}/I_{1E} = -N_1(I_{1E})/N_2(I_{2E})$ for broken PT symmetry result in the IHSS equilibrium as

$$I_{1E} = -\frac{1}{\eta_{11}}\left(\frac{\kappa^2}{\eta_{20}} + \eta_{10} \right), \quad I_{2E} = -\frac{\kappa^2}{\eta_{11}\eta_{20}^2}\left(\frac{\kappa^2}{\eta_{20}} + \eta_{10} \right). \tag{S15}$$

The Jacobian eigenvalues for the equilibrium are then achieved as

$$\lambda_{\pm E} = -\eta_{10} + \frac{\eta_{20}}{2} - \frac{3}{2}\frac{\kappa^2}{\eta_{20}} \pm \frac{1}{2}\sqrt{\left(2\eta_{10} + \eta_{20} + 3\frac{\kappa^2}{\eta_{20}} \right)^2 - 4\kappa^2}. \tag{S16}$$

NOTE I. EQUILIBRIA IN THE TPA EXAMPLE

Figure S3 shows the equilibria of unbroken (Fig. S3a, I_{HE}) and broken (Fig. S3b and c, each for I_{1E} and I_{2E}) PT symmetry. In the parameter space η_{10}-η_{20}, the nontrivial equilibria exist except for the gray areas, which represent the "forbidden regions" of nontrivial equilibria. First, due to the necessary condition $\kappa \geq |\eta_{20}|$ for unbroken PT symmetry, the equilibrium in Fig. S3a is defined only in the range of $-1 \leq (\eta_{20} / \kappa) \leq 1$, while broken PT symmetry is automatically satisfied with the equilibrium condition $N_1(I_{1E})N_2(I_{2E}) = -\kappa^2$. The other forbidden regions

originate from negative intensity values ($I_{HE} < 0$ and $I_{1E,2E} < 0$). The equilibrium in broken PT symmetry satisfies $I_{1E} \neq I_{2E}$ except for $\kappa = |\eta_{20}|$ shown in Eq. (S15), leading to IHSS equilibria.

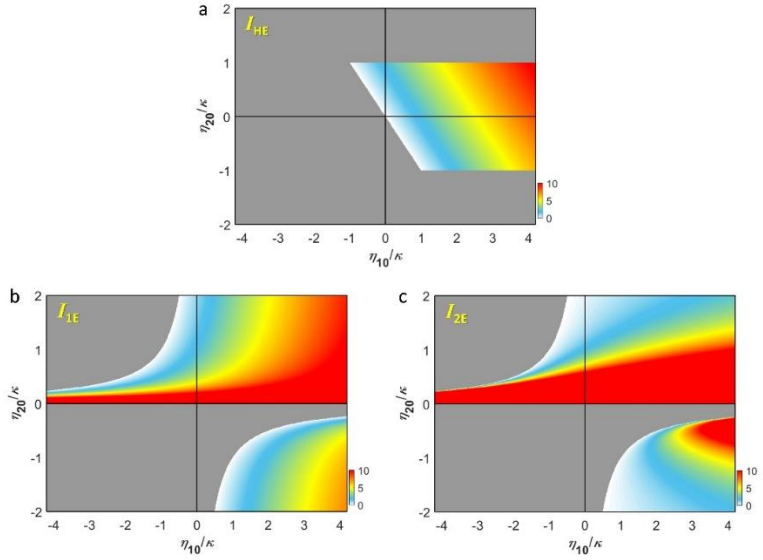

Fig. S3. Equilibria in the system parameter space η_{10}-η_{20}. (a) I_{HE} for unbroken PT symmetry. (b) I_{1E} and (c) I_{2E} for broken PT symmetry. The gray areas denote the forbidden regions, originating from unbroken PT symmetry and nonnegative intensity values. $\eta_{11}/\kappa = -0.5$.

NOTE J. JACOBIAN EIGENVALUES OF BROKEN PT SYMMETRY IN THE TPA EXAMPLE

Figure S4 shows the imaginary part of λ_{+E} (Fig. S4a) and complex-valued λ_{-E} (Fig. S4b and c) to provide all the information of $\lambda_{\pm E}$ for broken PT symmetry with Fig. 1d in the main text. In the region of $\eta_{20} / \kappa > 0$ except for the forbidden region (gray color), the saddle (D) phase of $(n_+,n_-) = (1,1)$ consists of $\mathrm{Re}[\lambda_{+E}] < 0$ (Fig. 1d in the main text) with $\mathrm{Im}[\lambda_{+E}] = 0$ and $\mathrm{Re}[\lambda_{-E}] > 0$ with $\mathrm{Im}[\lambda_{-E}] = 0$.

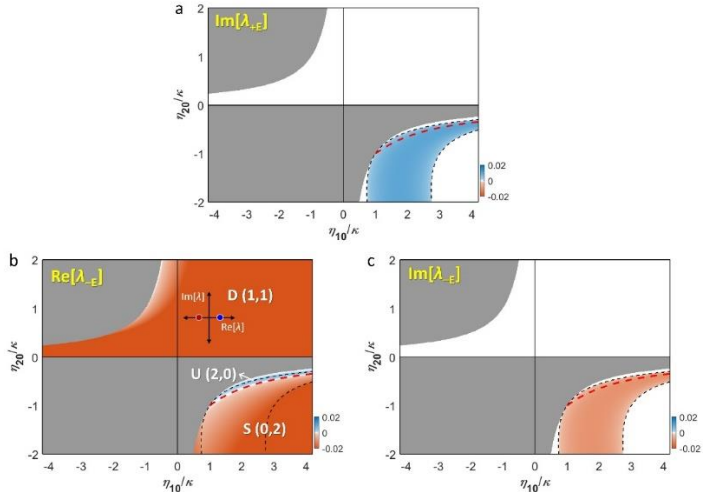

Fig. S4. Complex-valued Jacobian eigenvalues. (a) $\mathrm{Im}[\lambda_{+E}]$, (b) $\mathrm{Re}[\lambda_{-E}]$, and (c) $\mathrm{Im}[\lambda_{-E}]$. The red lines denote the AH bifurcation, and the black dashed lines represent the boundaries between the node and focus phases. $\eta_{11}/\kappa = -0.5$ for all cases.

The S and U phases in the region of $\eta_{20} / \kappa < 0$ can be further classified by the types of phase portraits (Fig. S5): node (S^N and U^N) and focus (S^F and U^F) phases, which are topologically equivalent [16] if the phases have the same (n_+,n_-). While node phases have Jacobian eigenvalues on the real axis, focus phases have a complex-conjugate pair of eigenvalues. It is noted that the AH bifurcation occurs only between the focus phases S^F and U^F.

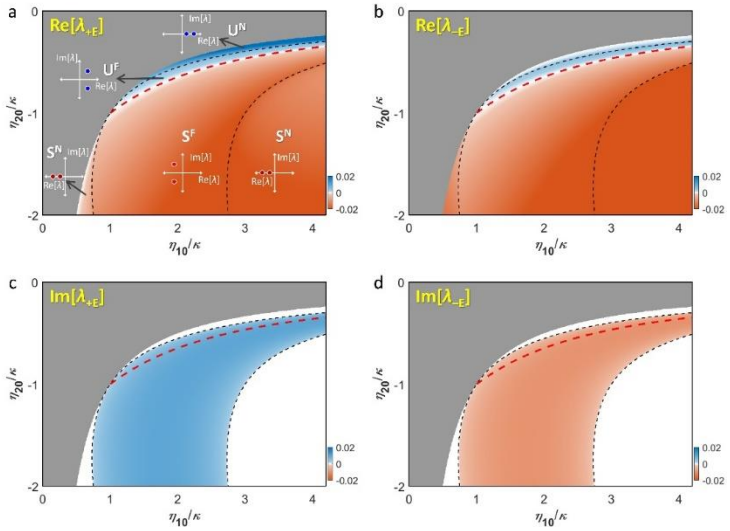

Fig. S5. Node-focus classifications in the S and U phases. (a) Re[λ_{+E}], (b) Re[λ_{-E}], (c) Im[λ_{+E}], and (d) Im[λ_{-E}]. The red lines denote the AH bifurcation, and the black dashed lines represent the boundaries between the node and focus phases. $\eta_{11}/\kappa = -0.5$.

NOTE K. THE TPE EXAMPLE

We also analyze photonic molecules with the TPE nonlinearity having $\eta_{11} > 0$ (Figs. S6 and S7), which lead to a topological classification that contrasts with the TPA example: a single U(1,0) phase in unbroken PT symmetry and broad U(2,0) and narrow S(0,2) phases in broken PT symmetry. As shown in the analytical solutions $\lambda_{HE} = -(\eta_{10} + \eta_{20})$ and $\lambda_{\pm E}$ in Eq. (S16), the Jacobian eigenvalues in unbroken and broken PT symmetry are independent of η_{11}. Instead, the values of the equilibria I_{HE} and $I_{1E,2E}$ depend on η_{11}, which determines the forbidden regions of nontrivial equilibria from negative intensity values ($I_{HE} < 0$ and $I_{1E,2E} < 0$) and thus results in differences between the topological phases of the TPE and TPA photonic molecules.

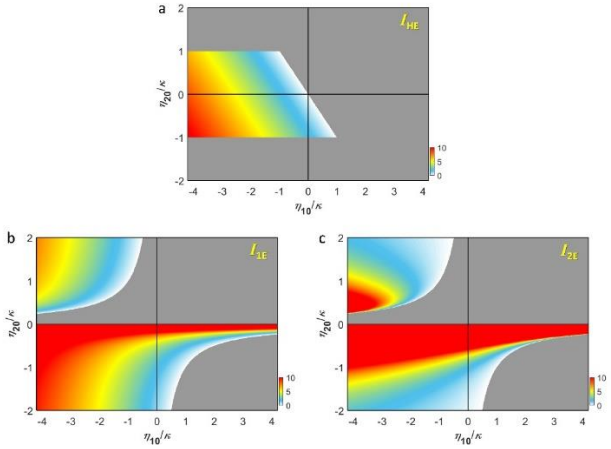

Fig. S6. Equilibria of TPE photonic molecules in the system parameter space η_{10}-η_{20}. (a) I_{HE} for unbroken PT symmetry. (b) I_{1E} and (c) I_{2E} for broken PT symmetry. The gray areas denote the forbidden regions of nontrivial equilibria. $\eta_{11}/\kappa = +0.5$ for all cases.

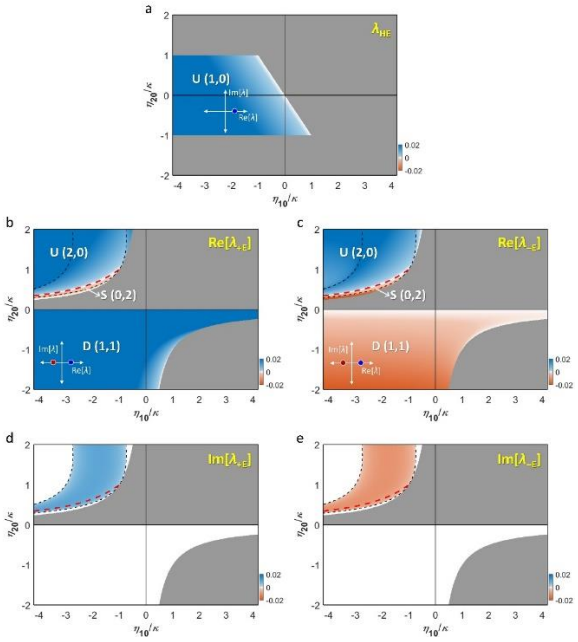

Fig. S7. Topological classification of TPE photonic molecules. (a) λ_{HE} for unbroken PT symmetry. (b) Re[λ_{+E}], (c) Re[λ_{-E}], (d) Im[λ_{+E}], and (e) Im[λ_{-E}] for broken PT symmetry. The red lines denote the AH bifurcation, and the black dashed lines represent the boundaries between the node and focus phases. $\eta_{11}/\kappa = +0.5$ for all cases.

NOTE L. TOPOLOGICALLY PROTECTED DYNAMICS IN THE SADDLE AND UNSTABLE PHASES

The phase portraits in the saddle and unstable phases are presented in Fig. S8. While Fig. S8a shows the saddle phase dynamics obtained with the TPA resonator ($\eta_{11} < 0$), Fig. S8b and c represent the unstable dynamics obtained with TPE resonators ($\eta_{11} > 0$). Although both phases are unstable with respect to the nontrivial equilibrium, some of the initial states can converge to $(I_{1E},I_{2E}) = (0,0)$, depending on the topological phase of the trivial equilibrium (0,0).

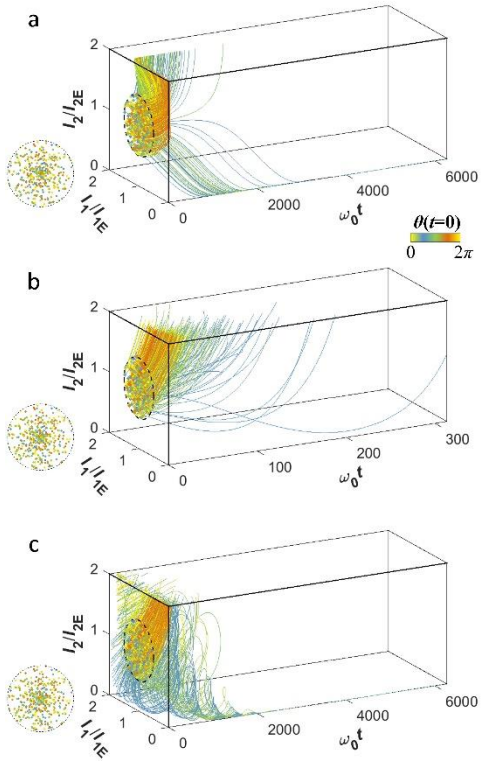

Fig. S8. Phase portraits of the saddle and unstable topological phases. (a-c) Trajectories of (I_1,I_2). (a) D(1,1) phase with broken PT symmetry where $(\eta_{10}/\kappa, \eta_{20}/\kappa) = (–1.0, 0.5)$ and $\eta_{11}/\kappa = –0.5$. (b) U(0,2) phase with broken PT symmetry where $(\eta_{10}/\kappa, \eta_{20}/\kappa) = (–2.0, 1.5)$ and $\eta_{11}/\kappa = +0.5$. (c) U(0,1) phase with unbroken PT symmetry where $(\eta_{10}/\kappa, \eta_{20}/\kappa) = (–1.0, 0.5)$ and $\eta_{11}/\kappa = +0.5$. All other parameters are the same as those in Fig. 2 in the main text.

NOTE M. TEMPORAL SYSTEM PERTURBATIONS

To examine the effect of noise time scales on topological protection, we introduce temporal system perturbations that are realized by adding random square pulses $\Delta\eta_{10}(t)$ and $\Delta\eta_{20}(t)$ to $(\eta_{10}/\kappa, \eta_{20}/\kappa) = (1.0, -0.5)$ for the S(0,1) phase and $(\eta_{10}/\kappa, \eta_{20}/\kappa) = (2.0, -1.5)$ for the S(0,2) phase, forming $\eta_{10}(t)$ and $\eta_{20}(t)$ (Fig. S9). For the analysis in Supplementary Note N, the square pulse is defined by the widths t_{width}, intervals t_{interval}, and amplitudes $\Delta\eta$ of the square pulses, which are defined by the uniform random distribution $u[p,q]$ between p and q.

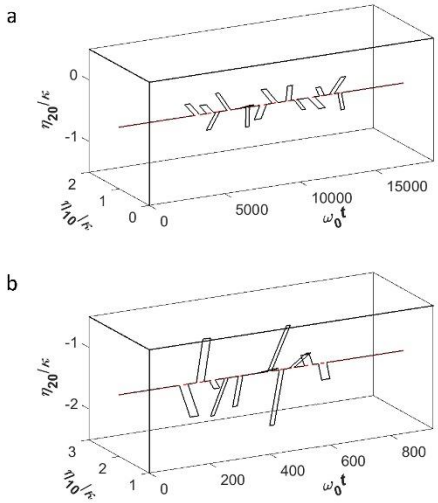

Fig. S9. An example of temporal variations in the system perturbations. (a,b) $\eta_{10}(t)$ and $\eta_{20}(t)$ for the (a) S(0,1) phase and (b) S(0,2) phase.

NOTE N. TIME SCALES OF SYSTEM PERTURBATIONS

We examine the effect of the time scale of system perturbations in the topological protection at the S(0,1) and S(0,2) phases. The time scale is controlled with the widths of the square pulses for $\eta_{10}(t)$ and $\eta_{20}(t)$. As shown, the perturbation with larger time scales leads to the stronger deviation of (I_1,I_2) from the original equilibrium point (I_{1E},I_{2E}), though the topological protection is eventually achieved when the original system parameters are recovered.

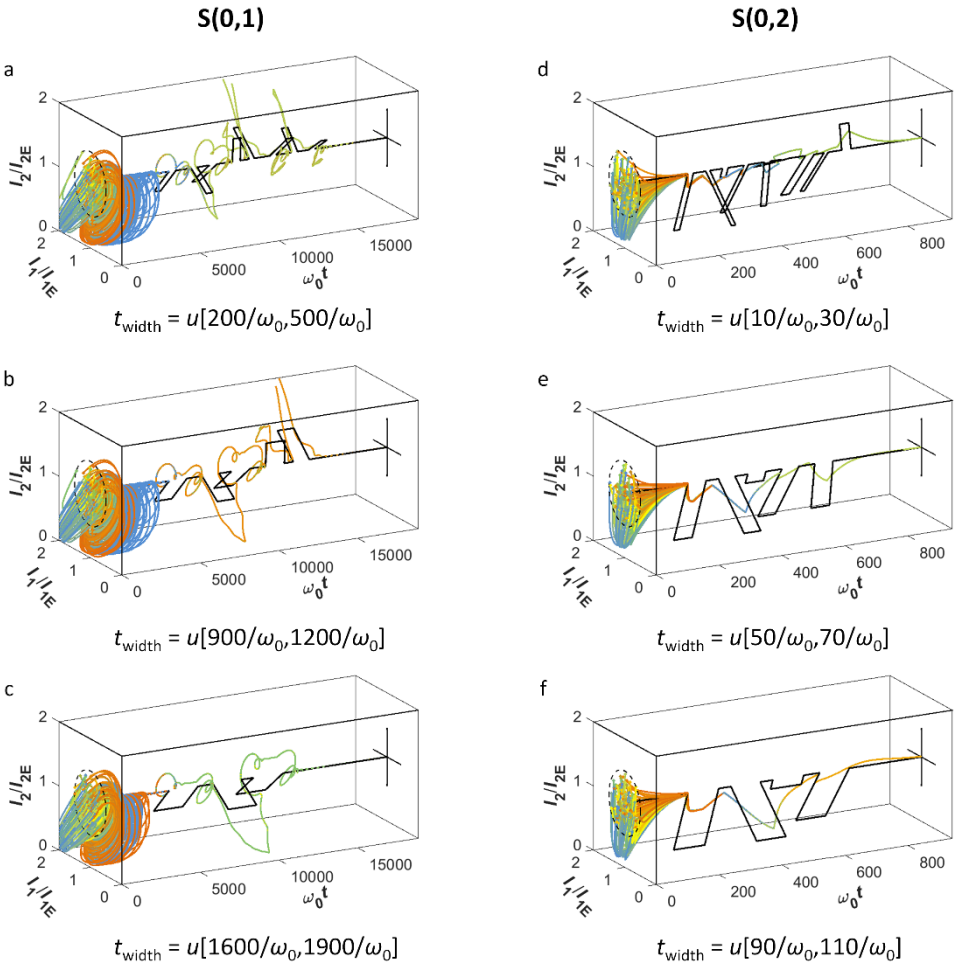

Fig. S10. Effects of the time scale of noises on their suppression based on topologically protection. Trajectories of (I_1,I_2) for the (a-c) S(0,1) phase around $(\eta_{10}/\kappa, \eta_{20}/\kappa) = (1.0, -0.5)$ and (d-f) S(0,2) phase around $(\eta_{10}/\kappa, \eta_{20}/\kappa) = (2.0, -1.5)$. S(0,1) phase: (a) $t_{width} = u[200/\omega_0,500/\omega_0]$, (b) $t_{width} = u[900/\omega_0,1200/\omega_0]$, and (c) $t_{width} = u[1600/\omega_0,1900/\omega_0]$, with $t_{interval} = u[500/\omega_0,1000/\omega_0]$ and $\Delta\eta = u[-0.4\kappa,+0.4\kappa]$. S(0,2) phase: (a) $t_{width} = u[10/\omega_0,30/\omega_0]$, (b) $t_{width} = u[50/\omega_0,70/\omega_0]$, and (c) $t_{width} = u[90/\omega_0,110/\omega_0]$, with $t_{interval} = u[30/\omega_0,60/\omega_0]$ and $\Delta\eta = u[-1.0\kappa,+1.0\kappa]$.

NOTE O. TEMPORAL COUPLED MODE THEORY FOR A LASER PLATFORM

The TCMT formulation for the platform of Figs. 4 and 5 in the main text is

$$\frac{da_1}{dt} = i\omega_0 a_1 + \left[N_1\left(|a_1|^2\right) - \frac{1}{\tau_W} \right] a_1 + i\kappa a_2 + \sqrt{\frac{2}{\tau_W}} S_{1+},$$
$$\frac{da_2}{dt} = i\omega_0 a_2 + \left[N_2\left(|a_2|^2\right) - \frac{1}{\tau_W} \right] a_2 + i\kappa a_1 + \sqrt{\frac{2}{\tau_W}} S_{2+}, \quad \text{(S17)}$$

where $S_{1+,2+}$ denote the incident waves through each waveguide. The emitted waves $S_{1-,2-}$ from the nonlinear photonic molecule are obtained as

$$S_{1-} = -S_{1+} + \sqrt{\frac{2}{\tau_W}} a_1,$$
$$S_{2-} = -S_{2+} + \sqrt{\frac{2}{\tau_W}} a_2. \quad \text{(S18)}$$

The incident waves $S_{1+,2+}$ are used for the initial excitation of the nonlinear photonic molecule. We thus set $S_{1+,2+} \sim 0$ after a sufficient time from the excitation. Equation (S17) then takes the form of Eq. (1) in the main text with the transformed nonlinearity functions $N_1(I_1) = \eta_{11} I_1 + \eta_{10} - 1/\tau_W$ and $N_2(I_2) = \eta_{20} - 1/\tau_W$. Accordingly, the topological phases in Fig. 1 in the main text are achieved by assigning an additional linear gain of $1/\tau_W$ to each resonator. Additionally, the emitted wave intensities are obtained as $|S_{1-,2-}|^2 = (2/\tau_W)|a_{1,2}|^2$ near the equilibrium with $S_{1+,2+} \sim 0$. Therefore, amplitude death (AD) and OD in each topological phase are successfully manifested in the emission intensities $|S_{1-,2-}|^2$.

NOTE P. NOISE IN TIME-VARYING LOSS

In the time domain analysis in Figs. 4 and 5 in the main text, sinusoidal and square pulses including noise components are applied to test noise-immune laser rectification and modulation, respectively. For the target signal $f_{target}(t)$ (square pulse in Fig. 4b and sinusoidal pulse in Fig. 5b in the main text), we set the modulation input $\eta_{20}(t)$ by adding a random perturbation $\delta_{20}(t)$ to $f_{target}(t)$ as $\eta_{20}(t) = f_{target}(t) + \delta_{20}(t)$, where:

$$\delta_{20}(t) = \int_W u[0,\delta] \cos(\omega t + u[-\pi,\pi]) d\omega, \quad \text{(S19)}$$

$W = [\omega_L, \omega_H]$ is the spectral bandwidth of the noise component, and $u[p,q]$ is the uniform random function. The strength of the noise is then determined by the magnitude of δ (Fig. S11a for Figs. 4c and 5c, and Fig. S11b for Figs. 4d and 5d). In both examples, $\omega_L = 0.1\omega_0$ and $\omega_H = 0.2\omega_0$.

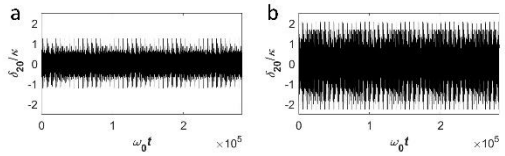

Fig. S11. Noise components $\delta_{20}(t)$ defined by the uniform random function and the magnitude δ. (a) $\delta = 77.5 / \omega_0$ and (b) $\delta = 155 / \omega_0$.

NOTE Q. NOISE-IMMUNE OPERATION FOR SLOWER PERTURBATIONS

Figure S12 shows the effect of noise rates on noise-immune signal processing performance. For the square pulses including noise components (Supplementary Note P), we estimate the noise immunity in signal modulation for different values of $W = [\omega_L, \omega_H]$: the spectral bandwidth of the noise component. As demonstrated, better noise suppression is achieved with faster system perturbations because slower noises operate as "signals" according to the dynamical evolution of the equilibrium point (I_{1E}, I_{2E}) and the sufficient convergence to each changed equilibrium.

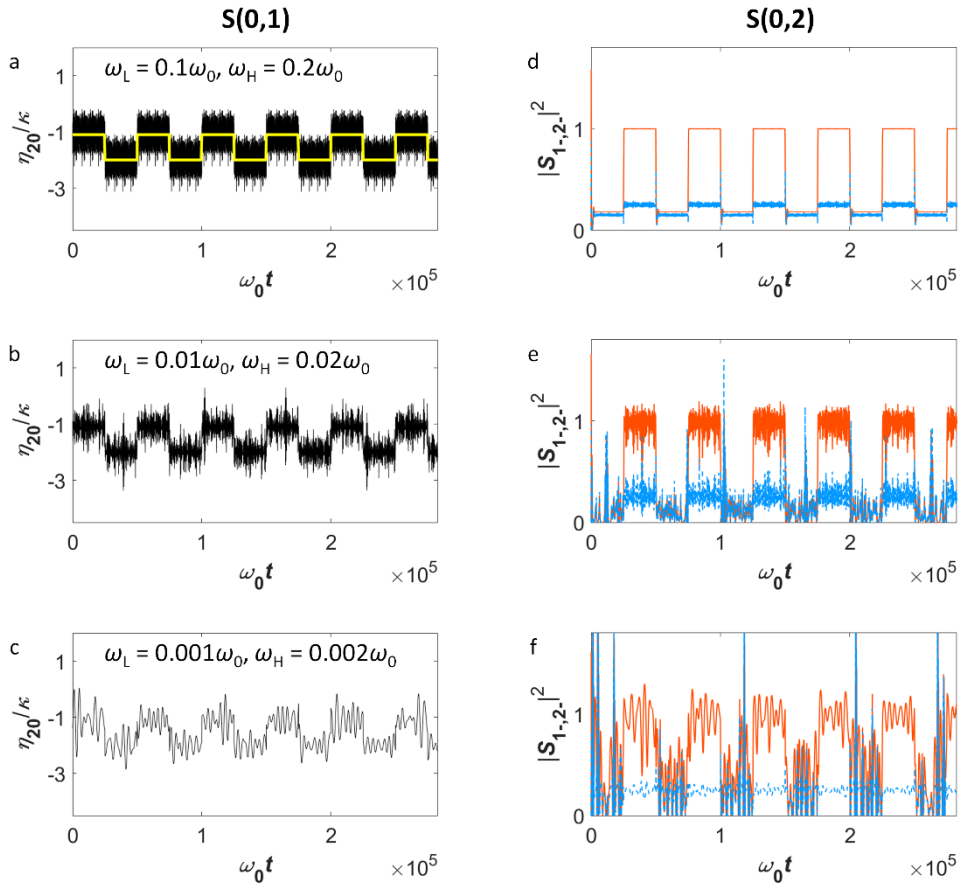

Fig. S12. Effect of noise rates on noise-immune signal processing. (a-c) κ-normalized modulation signals $\eta_{20}(t)$ with different spectral bandwidths W and (d-f) the corresponding output signals $|S_{1-}|^2$ and $|S_{2-}|^2$. (a,d) $\omega_L = 0.1\omega_0$ and $\omega_H = 0.2\omega_0$. (b,e) $\omega_L = 0.01\omega_0$ and $\omega_H = 0.02\omega_0$. (c,f) $\omega_L = 0.001\omega_0$ and $\omega_H = 0.002\omega_0$. All other parameters are the same as those in Fig. 4 in the main text.

Supplementary References

1. L. Chang, X. Jiang, S. Hua, C. Yang, J. Wen, L. Jiang, G. Li, G. Wang, and M. Xiao, "Parity–time symmetry and variable optical isolation in active–passive-coupled microresonators," Nat. Photon. **8**, 524-529 (2014).
2. E. Spiller, "Saturable optical resonator," J. Appl. Phys. **43**, 1673-1681 (1972).
3. B. Wherrett, "Scaling rules for multiphoton interband absorption in semiconductors," J. Opt. Soc. Am. B **1**, 67-72 (1984).
4. Y. Shen, "Quantum statistics of nonlinear optics," Phys. Rev. **155**, 921 (1967).
5. H. K. Tsang, C. Wong, T. Liang, I. Day, S. Roberts, A. Harpin, J. Drake, and M. Asghari, "Optical dispersion, two-photon absorption and self-phase modulation in silicon waveguides at 1.5 μ m wavelength," Appl. Phys. Lett. **80**, 416-418 (2002).
6. Z. Wang, H. Liu, N. Huang, Q. Sun, J. Wen, and X. Li, "Influence of three-photon absorption on mid-infrared cross-phase modulation in silicon-on-sapphire waveguides," Opt. Express **21**, 1840-1848 (2013).
7. A. Nevet, N. Berkovitch, A. Hayat, P. Ginzburg, S. Ginzach, O. Sorias, and M. Orenstein, "Plasmonic nanoantennas for broad-band enhancement of two-photon emission from semiconductors," Nano Lett. **10**, 1848-1852 (2010).
8. C. S. Muñoz, E. Del Valle, A. G. Tudela, K. Müller, S. Lichtmannecker, M. Kaniber, C. Tejedor, J. Finley, and F. Laussy, "Emitters of N-photon bundles," Nat. Photon. **8**, 550 (2014).

9. L. Yang, T. Carmon, B. Min, S. M. Spillane, and K. J. Vahala, "Erbium-doped and Raman microlasers on a silicon chip fabricated by the sol–gel process," Appl. Phys. Lett. **86**, 091114 (2005).
10. Q. Bao, H. Zhang, Y. Wang, Z. Ni, Y. Yan, Z. X. Shen, K. P. Loh, and D. Y. Tang, "Atomic-layer graphene as a saturable absorber for ultrafast pulsed lasers," Adv. Funct. Mater. **19**, 3077-3083 (2009).
11. M. Teimourpour, A. Rahman, K. Srinivasan, and R. El-Ganainy, "Non-Hermitian Engineering of Synthetic Saturable Absorbers for Applications in Photonics," Phys. Rev. Appl. **7**, 014015 (2017).
12. C. E. Rüter, K. G. Makris, R. El-Ganainy, D. N. Christodoulides, M. Segev, and D. Kip, "Observation of parity–time symmetry in optics," Nat. Phys. **6**, 192-195 (2010).
13. R. El-Ganainy, K. G. Makris, M. Khajavikhan, Z. H. Musslimani, S. Rotter, and D. N. Christodoulides, "Non-Hermitian physics and PT symmetry," Nat. Phys. **14**, 11-19 (2018).
14. G. Saxena, A. Prasad, and R. Ramaswamy, "Amplitude death: The emergence of stationarity in coupled nonlinear systems," Phys. Rep. **521**, 205-228 (2012).
15. A. Koseska, E. Volkov, and J. Kurths, "Oscillation quenching mechanisms: Amplitude vs. oscillation death," Phys. Rep. **531**, 173-199 (2013).
16. Y. A. Kuznetsov, *Elements of applied bifurcation theory* (Springer Science & Business Media, Berlin, Germany, 2013), Vol. 112.